On the advantages of spring magnets compared to pure FePt: Strategy for rare-earth free permanent magnets following a bottom-up approach

Marc Pousthomis, Cyril Garnero, Cécile Marcelot, Thomas Blon, Simon Cayez, C. Cassignol, V.A. Du, M. Krispin, R. Arenal, Aikaterini Soulantika, et al.

HAL Id: hal-01982650

https://hal.insa-toulouse.fr/hal-01982650

Submitted on 15 Jan 2019

Author's Accepted Manuscript

On the advantages of spring magnets compared to pure FePt : strategy for rare-earth free permanent magnets following a bottom-up approach

M Pousthomis, C Garnero, C G Marcelot, T Blon, S Cayez, C Cassignol, V A Du, M Krispin, R Arenal, K Soulantica, G Viau, L-M Lacroix
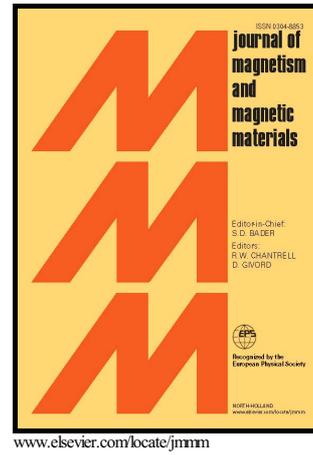
Cite this article as: M Pousthomis, C Garnero, C G Marcelot, T Blon, S Cayez, C Cassignol, V A Du, M Krispin, R Arenal, K Soulantica, G Viau and L-M Lacroix, On the advantages of spring magnets compared to pure FePt : strategy for rare-earth free permanent magnets following a bottom-up approach, *Journal of Magnetism and Magnetic Materials* http://dx.doi.org/10.1016/j.jmmm.2016.10.071

This is a PDF file of an unedited manuscript that has been accepted for publication. As a service to our customers we are providing this early version of the manuscript. The manuscript will undergo copyediting, typesetting, and review of the resulting galley proof before it is published in its final citable form. Please note that during the production process errors may be discovered which could affect the content, and all legal disclaimers that apply to the journal pertain.

On the advantages of spring magnets compared to pure FePt : strategy for rare-earth free permanent magnets following a bottom-up approach

M Pousthomis[1], C Garnero[1], C G Marcelot[1,2], T Blon[1], S Cayez[1], CCassignol[3], V A Du[3], M Krispin[3], R Arenal[4,5,6], K Soulantica[1], G Viau[1], L-M Lacroix[1,4*]

[1]Université de Toulouse, UMR 5215 INSA, CNRS, UPS, Laboratoire de Physique et Chimie des Nano-Objets, 135 avenue de Rangueil F-31077 Toulouse cedex 4, France
[2]Centre d'Elaboration de Matériaux et d'Etudes Structurales, CEMES-CNRS, 29 rue Jeanne Marvig, B.P. 94347, 31055 Toulouse, France
[3]Siemens AG, Corporate Technology, Munich, Germany
[4]Transpyrenean Advanced Laboratory for Electron Microscopy (TALEM), INSA - INA, CNRS - Universidad de Zaragoza, 30155 Toulouse, France
[5]Laboratorio de Microscopias Avanzadas (LMA), Instituto de Nanociencia de Aragon (INA), U. Zaragoza, C/ Mariano Esquillor s/n, 50018 Zaragoza (Spain).
[6]Fundacion ARAID, 50018 Zaragoza, Spain.

Corresponding author : lmlacroi@insa-toulouse.fr, Tel : +33567048833, Fax : +33561559697

Abstract :

Nanostructured magnets benefiting from efficient exchange-coupling between hard and soft grains represent an appealing approach for integrated miniaturized magnetic power sources. Using a bottom-up approach, nanostructured materials were prepared from binary assemblies of *bcc* FeCo and *fcc* FePt nanoparticles and compared with pure $L1_0$-FePt materials. The use of a bifunctional mercapto benzoic acid yields homogeneous assemblies of the two types of particles while reducing the organic matter amount. The 650°C thermal annealing, mandatory to allow the $L1_0$-FePt phase transition, led to an important interdiffusion and thus decreased drastically the amount of soft phase present in the final composites. The analysis of recoil curves however evidenced the presence of an efficient interphase exchange coupling, which allows obtaining better magnetic performances than pure $L1_0$ FePt materials, energy product above 100 kJ.m^{-3} being estimated for a Pt content of only 33%. These results clearly evidenced the interest of chemically grown nanoparticles for the preparation of performant spring-magnets, opening promising perspective for integrated subcentimetric magnets with optimized properties.

1. Introduction

High potential applications such as Micro-Electro-Mechanical Systems (MEMS) and the derived biosensors require sub-centimetric permanent magnets with high remanent induction (B_r) and energy product ($(BH)_{max}$) [1]. Indeed, the magnetic flux density available, being independent of the size, permanent magnets represent the most attractive choice for miniaturized magnetic power sources [2]. Three main categories of permanent magnets are nowadays available, the ferrite based-magnets, which are by far the cheapest but exhibit poor properties ($(BH)_{max}$ ~ 10-30 kJ/m^3), the AlNiCo magnets with intermediate properties (40-80 kJ/m^3), and the highly performant rare earth-based (RE) magnets (120 - 400 kJ/m^3) [3]. For MEMS applications energy products above 100 kJ/m^3 should be targeted, limiting so far the choice to RE-magnets. However, their fabrication and integration into predefined circuits remains highly challenging. Thus, important efforts are devoted to: i) materials, which should fill the gap between AlNiCo and RE magnets without suffering from corrosion issues, and ii) processes which should be redefined to be scalable down to submillimeter sizes, contrarily to the classical metallurgic processes used.

Exchange coupling between soft and hard phases, providing respectively a high saturation magnetization (Ms) and a large anisotropy (K), could fulfil both objectives of performance and integration [4]. For the FeCo alloy, which exhibits one of the highest saturation magnetization ($\mu_0 M_S =$ 2.4 T), $(BH)_{max}$ values of 1150 kJ/m^3 could be theoretically obtained, providing a sufficient anisotropy ($K > 5 \times 10^6$ J/m^3). This latter value is however two orders of magnitude above the intrinsic properties of FeCo ($K = 2 \times 10^4$ J/m^3) [5]. Coupling bcc-FeCo with hard phases such as $L1_0$-FePt ($K = 6.6 \times 10^6$ J/m^3) [6] could allow one to fully benefit from the potential $(BH)_{max}$.

However, for the exchange coupling to be effective, a fine tuning of the nanocomposite microstructure is required [7] :

- The characteristic dimensions of the soft phase grains should not exceed a critical size (D_{mc}) to prevent magnetic decoupling and the apparition of a two-step hysteresis curve.[8,9] This critical size

depends on intrinsic parameters of hard and soft grains and is typically in the order of few tens of nm.[10,11,12]

- The grain size of the hard phase should also be lowered to the same extent to allow a high volume fraction of the soft phase, and thus, a high magnetization of the nanocomposite [9,13]. Consequently the best expected microstructure consists in small hard phase grains densely distributed within in a soft matrix [4,8].

Since the pioneer works on exchange coupled nanomagnets [4,14] and the giant energy products predicted [4,8], intensive researches have been dedicated to their elaboration by various approaches. Conventional metallurgic approaches, [15,16] such as ball milling or melt spinning, led to fairly broad grain size distribution, and thus non optimized exchange coupling. On the contrary, *sputtering* deposition [7,17,18,19] allows to finely tune the hard and soft grain sizes, leading to the highest $(BH)_{max}$ ever reported (405 kJ/m^3) for magnetically aligned biphasic grains of $L1_0$-FePt and *fcc* Fe$_3$Pt [20].

An alternative relies on the self-assembly of chemically grown building blocks. This bottom-up approach was successfully demonstrated in 2002 by IBM researchers, mixing 4 nm *fcc* Fe$_{58}$Pt$_{42}$ with 4 nm Fe$_3$O$_4$ nanoparticles (NPs) [21]. An optimum mass fraction of Fe$_3$O$_4$ of only 10% was determined and led, after thermal annealing at 650°C under Ar- 5% H$_2$ atmosphere, to exchange-coupled $L1_0$-FePt/$L1_2$-Fe$_3$Pt grains exhibiting $(BH)_{Max}$ values of 160 kJ/m^3. Though highly promising, the high amount of Pt (~45% at.) present in the final magnets limited their industrial applications. Neither the optimization of the soft/hard interphase [22,23,24,25], nor the optimization of the consolidation process [17,26] could so far reduce the Pt amount without altering the properties of the magnet.

We report here a systematic study of the assembly and thermal annealing of chemically grown FeCo and FePt nanoparticles. The structural and magnetic properties of the obtained composites are compared to pure FePt materials, highlighting the beneficial impact of the soft phase, high $(BH)_{max}$ ($\geq$ 100 kJ/m^3) being estimated, even at low Pt content (33% atomic).

3

2. Methods

2.1. FeCo NPs synthesis

6 nm $Fe_{50}Co_{50}$ NPs were synthesized using an adapted organometallic approach [27]. Briefly, Fe and Co silylamides, $(Fe[N\{Si(CH_3)_3\}_2]_2)_2$ and $Co[N\{Si(CH_3)_3\}_2]_2(THF)$ were reduced under 3 bars of H_2 at 150°C for 48h in mesitylene and in the presence of long chain surfactants (hexadecylamine – HDA, and palmitic acid - PA). The precursor concentrations were kept at 20 mmol/L. HDA and PA concentrations used were 80 mmol/L and 55 mmol/L respectively. After reaction, the excess of surfactant was removed by magnetically assisted separation under inert atmosphere to prevent any oxidation and the particles were kept as a powder in the glove box.

2.2. FePt NPs synthesis

Typically, 6 nm $Fe_{45}Pt_{55}$ NPs were obtained from the reduction of Pt and Fe acetylacetonate complexes at high temperature in an oleic acid/oleylamine mixture. $Fe(acac)_3$ (144 mg, 0,4 mmole) and $Pt(acac)_2$ (196 mg, 0,5 mmole) were added to a three neck flask containing 3.2 mL of oleic acid (10 mmole) and 16.8 mL of oleylamine (50 mmole). The system was purged for 30 min under Argon to remove any oxygen traces. The temperature was then increased up to 300°C with a heating rate of 7°C/min under Argon flow. After 1h of reaction, the solution was allowed to cool down to room temperature under an Argon blanket. The excess of surfactant was removed by 3 centrifugations (8min, 8000 rpm) using toluene as a solvent and absolute ethanol as a counter solvent. The particles were kept as a powder.

The composition of the FePt NPs could be tuned by adjusting the $Fe(acac)_3$ and $Pt(acac)_2$ amount introduced (table 1), all the other parameters were kept constant. The FePt particles will be referred to from now on as Rx, x indicating the atomic Pt content.

EDX Composition (%at.)	$Fe_{45}Pt_{55}$	$Fe_{52}Pt_{48}$ (R48)	$Fe_{55}Pt_{45}$	$Fe_{59}Pt_{41}$ (R41)	$Fe_{66}Pt_{34}$ (R34)
$Fe(acac)_3$	144 mg	177 mg	216 mg	211 mg	247 mg
$Pt(acac)_2$	196 mg	196 mg	196 mg	157 mg	118 mg

Table 1. Amount of $Fe(acac)_3$ and $Pt(acac)_2$ precursors initially introduced.

2.3. Binary assembly

Stable suspensions of $Fe_{45}Pt_{55}$ NPs and $Fe_{50}Co_{50}$ NPs were prepared by solubilizing each powder in tetrahydrofurane (THF). The two suspensions were mixed under ultrasonic agitation for 5 min. Ligand exchange was then performed on the homogeneous suspension obtained to reduce the organic matter and to prevent the formation of a detrimental carbon shell. Therefore, 4-mercaptobenzoic acid (MBA) was first solubilized in THF (4 mg/mL). The MBA solution was added onto the FeCo/FePt suspension to obtain a molar ratio of $MBA/Fe_{45}Pt_{55} = 1$. MBA was allowed to react 1 h at room temperature under mechanical stirring (500 rpm). The ligand excess was removed by 3 successive purifications, which consisted in centrifugation at 8000 rpm for 6 min and subsequent dispersion in THF. The particles were finally recovered in a small volume of THF and the solvent was evaporated to obtain a dry powder. Different FeCo/FePt ratios were targeted by adjusting the volumes of the starting solutions of FePt and FeCo NPs. The binary assemblies will be referred to from now on as Bx, x indicating the atomic Pt content.

2.4. Thermal annealing

The powders were placed in ceramic boats and annealed under forming gas (93% Ar, 7% H_2) in a tube furnace. A heating rate of 20°C/min was applied to reach the set temperature of 650°C. After 1h at 650°C, the powders were allowed to cool down to room temperature under forming gas.

2.5. Structural and morphological characterization

The two types of particles and the binary assemblies were characterized by transmission electron microscopy (TEM), using a 100kV Jeol JEM 1011 and high-angle annular dark-field scanning transmission electron microscopy (HAADF-STEM) using a 200 kV JEOL JEM 2100F and a FEI Titan Low-Base probe-corrected microscope working at 300 kV. For sample preparation, the particles were redispersed in toluene and a drop of the dispersion was deposited on a carbon coated copper grid.

Energy Dispersive X-Ray Spectroscopy (EDX) analyses were performed on powders deposited on a carbon tape using SDD Bruker detectors on a 30 kV JEOL JSM 7800F Scanning Electron Microscopy (SEM). Chemical composition has been determined using PB-ZAF corrections and averaged on 9

5

different areas. Chemical mapping have been performed using a 200 kV JEOL JSM 2100F and on a 300kV FEI Titan Low-Base TEMs. The Cliff-Lorimer correction, well suited for thin samples, was used.

Powders X-ray diffraction (XRD) patterns were recorded on a PANalytical Empyrean diffractometer using the Co K_α radiation.

To further characterize the efficiency of the *fcc* phase conversion *to L1$_0$*, the ordering factor S_1 of the tetragonal *L1$_0$* phase was determined for FePt and FePt-FeCo composites as :

$$S_1 = 0.85 \sqrt{\frac{I_{001}}{I_{002}}}. \qquad (2)$$

where I_{001} and I_{002} represent the intensity of the (001) and the (002) peak of the *L1$_0$* structure respectively [28].

2.6. Magnetic characterization

Magnetic measurements were performed using a Quantum Design Physical Property Measurement System (PPMS) in the Vibrating Sample Magnetometer (VSM) configuration. Powders were mixed with tetracosane to prevent the physical motion of the particles under magnetic solicitation, as previously described [29]. Manual compaction was performed to densify the powders. Hysteresis loops were recorded at 300K and 5K for applied magnetic fields varying between +/- 5T.

DC Demagnetization (DCD) measurements consists in determining the intermediate remanent magnetizations in the second and third quadrants of the major hysteresis loop by applying and releasing successive negative magnetic fields -H_i, to progressively demagnetize the material (figure 1). For each field –H_i, the two curves between H= –H_i and H=0 enclose a loop, known as recoil loop. While for conventional magnets the recoil curves are fairly flat, they become steeper in spring magnets due to the reversible rotation of the soft phase moments under external magnetic fields [4,7,15,30,31]. To quantitatively analyze the magnets, one can determine (i) the recoverable magnetization (M_{rec}), which represents the magnetization recovered along the recoil loops, (ii) the recoverable (χ_{rec}) and (iii) the reversible (χ_{rev}) susceptibilities, corresponding to the mean and local slope of the recoil loops

6

respectively (figure 1). For comparison purposes, these values have been normalized by the remanent magnetization M_r as follows :

$$m_{rec}(-Hi) = \frac{1}{M_r}(M_{rec}) = \frac{1}{M_r}(M(0) - M(-Hi)) \tag{3}$$

$$\chi_{rec}(-Hi) = \frac{1}{M_r}\frac{M_{rec}}{H_i} \tag{4}$$

$$\chi_{rev}(-Hi) = \frac{1}{M_r}\frac{\Delta M(-Hi)}{\Delta H} \tag{5}$$

where *M(0)* and *M(-Hi)* correspond to the intermediate remanent magnetization and the magnetization at the reversed field $-H_i$ respectively, while *ΔH* and *ΔM* represent a small variation of magnetic field (typically $\mu_0\Delta H = 100$ mT) and the corresponding variation of magnetization.
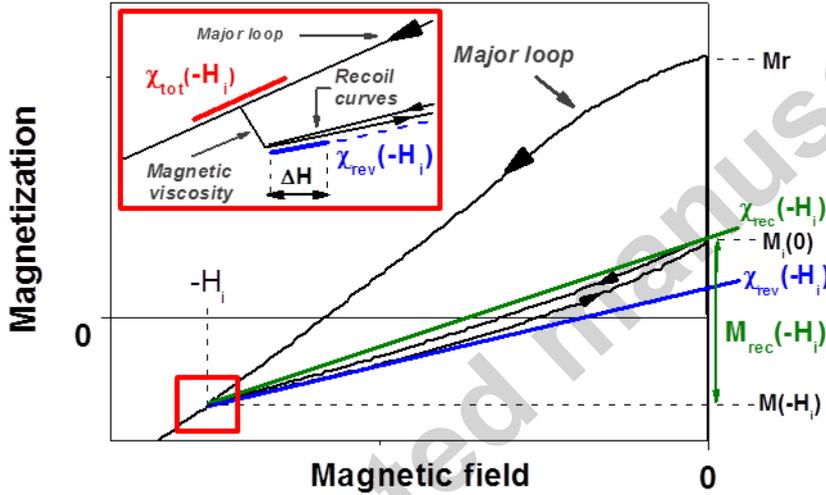

Figure 1. Schematic view of the DCD measurements, the M_{rec} recoverable magnetization and the different susceptibilities χ_{rev}, χ_{rec} and χ_{tot}.

DC Demagnetization measurements were performed on previously saturated samples by applying a negative magnetic field $-\mu_0 H_i$ at a speed of 10 mT/s. A 20 s delay was then applied to neglect magnetic viscosity before the field was reversed down to 0T, keeping the 10 mT/s speed [30]. The process was repeated until the negative saturation field -5T was reached. The reversible susceptibility at $-H_i$ was measured from the 10 first points of measurement on the recoil curve, corresponding to a field range of $\mu_0\Delta H \sim 100$ mT.

2.7. Evaluation of (BH)$_{max}$

B(H) loops were calculated from the M(H) loop considering dense materials and assuming that their densities can be calculated as the average of the volumic masses for each chemical element:

$$\rho\left(Fe_xCo_yPt_z\right) = f_{Fe}.\rho(Fe) + f_{Co}.\rho(Co) + f_{Pt}.\rho(Pt) \qquad (6)$$

where $\rho(i)$ and f_i correspond respectively to the volumic mass and to the volume fraction of the material i, with $\rho(Fe) = 7860$ kg.m^{-3}, $\rho(Co) = 8900$ kg.m^{-3} and $\rho(Pt) = 21450$ kg.m^{-3}.

The ideal volume magnetization could be deduced:

$$M(A.m^{-1}) = M(Am^2.kg^{-1}) * \rho\left(Fe_xCo_yPt_z\right) \qquad (7)$$

And the induction determined :

$$B(T) = \mu_0(H + M) \qquad (8)$$

3. Results

3.1. Characterization of the precursors

6nm Fe$_{45}$Pt$_{55}$ nanoparticles (NPs) were prepared by thermodecomposition of metal salts. They exhibit a fcc structure and a magnetization $M_{5T} = 30$ A.m^2.kg^{-1} (Figure S1 in SI). 6nm Fe$_{50}$Co$_{50}$ NPs were prepared following an organometallic approach. They exhibiting a bcc structure and a magnetization $M_{5T} = 220$ A.m^2.kg^{-1} (Figure S2 in SI). Assemblies of FeCo and FePt nanoparticles (NPs) were prepared by mixing the two types of particles in solution using tetrahydrofuran (THF) as solvent. TEM images of the solution obtained are presented in figure 2a-c and reveal a fairly homogeneous distribution of the two types of NPs, both stabilized by a mixture of acid and amine surfactants with long alkyl chains (length > 2nm). A ligand-exchange procedure was performed to reduce the amount of organic matter while promoting the binary assembly. 4-mercaptobenzoic acid (MBA), a short bi-functional molecule which combines carboxylic acid (R-COOH) and thiol (R-SH) functions, was used. Indeed, this ligand is known to bind strongly to the surface of the FePt NPs replacing long chain surfactants [32]. After MBA-ligand exchange, binary agglomerates were observed with smaller inter-NPs distances (figure 2d-f). The chemical compositions of the obtained assemblies were determined by SEM-EDX (table 2). Three samples, Fe$_{49}$Co$_6$Pt$_{45}$, Fe$_{48}$Co$_{12}$Pt$_{40}$ and Fe$_{50}$Co$_{17}$Pt$_{33}$, referred to from now on as B45, B40 and B33, were further characterized.
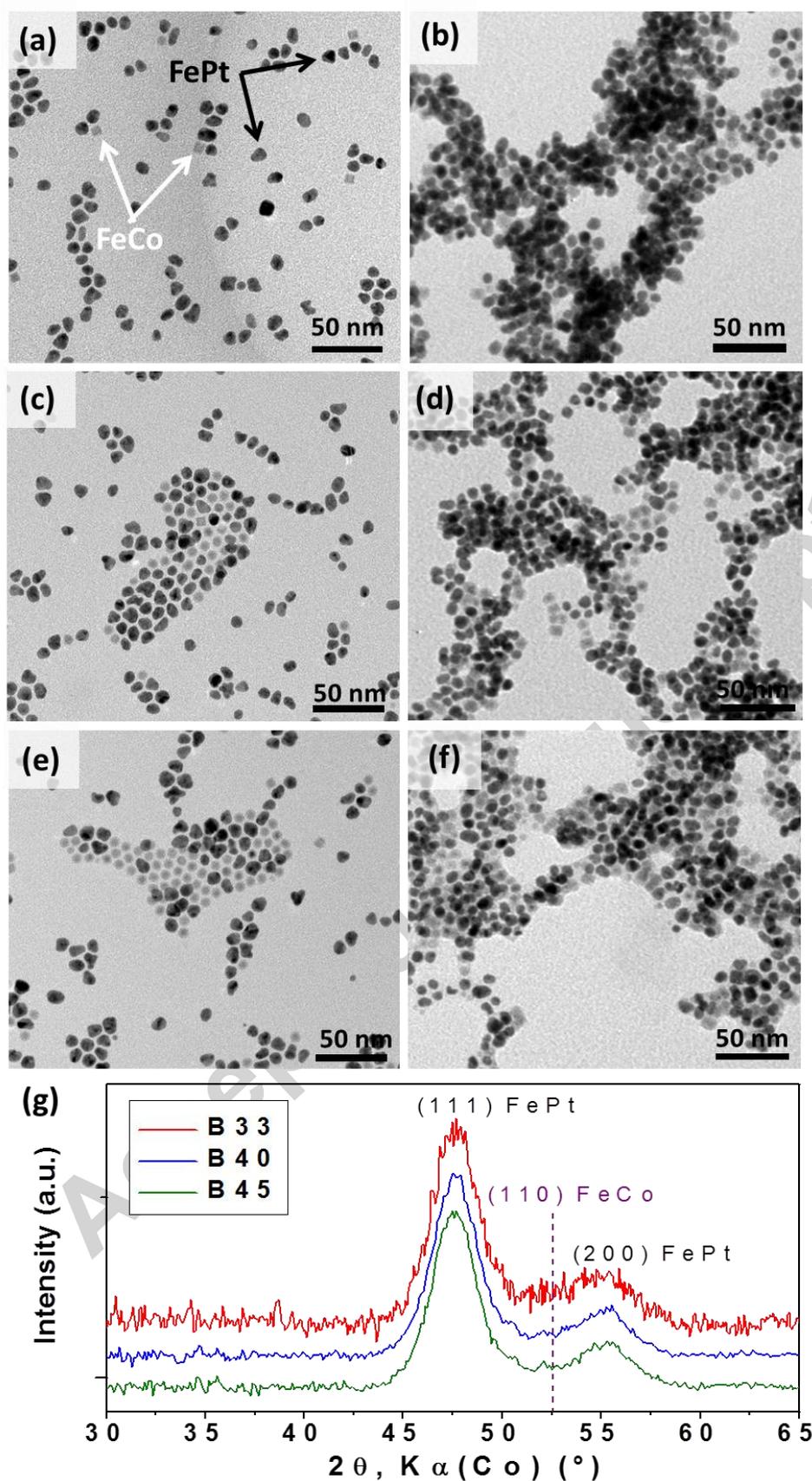
8

Figure 2. TEM images of binary assemblies (a), (b) B45, (c), (d) B40 and (e), (f) B33 and (g) the corresponding XRD patterns. Figures (a), (c) and (e) correspond to the binary assemblies in THF, figures (b), (d) and (f) correspond to the same assemblies after the addition of 1 eq. of MBA.

9

Chemical mapping of Fe, Pt and Co elements were performed using STEM-EDX technique (figure S3 in SI) revealing that the three elements are uniformly distributed.

XRD patterns evidence the presence of the *fcc* FePt phase, however the *bcc* FeCo phase could not be clearly detected, even for the highest FeCo content (figure 2g), the Pt atomic scattering factor being much higher than those of Fe and Co [33].

3.2. Characterizations after thermal annealing

3.2.1. Structural and chemical analysis. Thermal annealing at 650°C under forming gas was performed to promote the phase transition from the soft *fcc* FePt phase into the hard tetragonal ordered $L1_0$-FePt phase [34].

XRD patterns of five annealed samples $Fe_{100-x}Pt_x$ NPs, referred as Rx, where *x* represents the atomic Pt content expressed in percentage, are shown in figure 3a. For $x > 40\%$, the peaks attributed to $L1_0$-FePt phase were the only ones evidenced by XRD. On the contrary, for $x = 34\%$ (sample R34), the characteristic peaks of the $L1_2$-Fe$_3$Pt and an additional *bcc* phase were observed.

In the three binary assemblies, XRD patterns evidence only the presence of $L1_0$-FePt, even for the composite B33 (figure 3b).
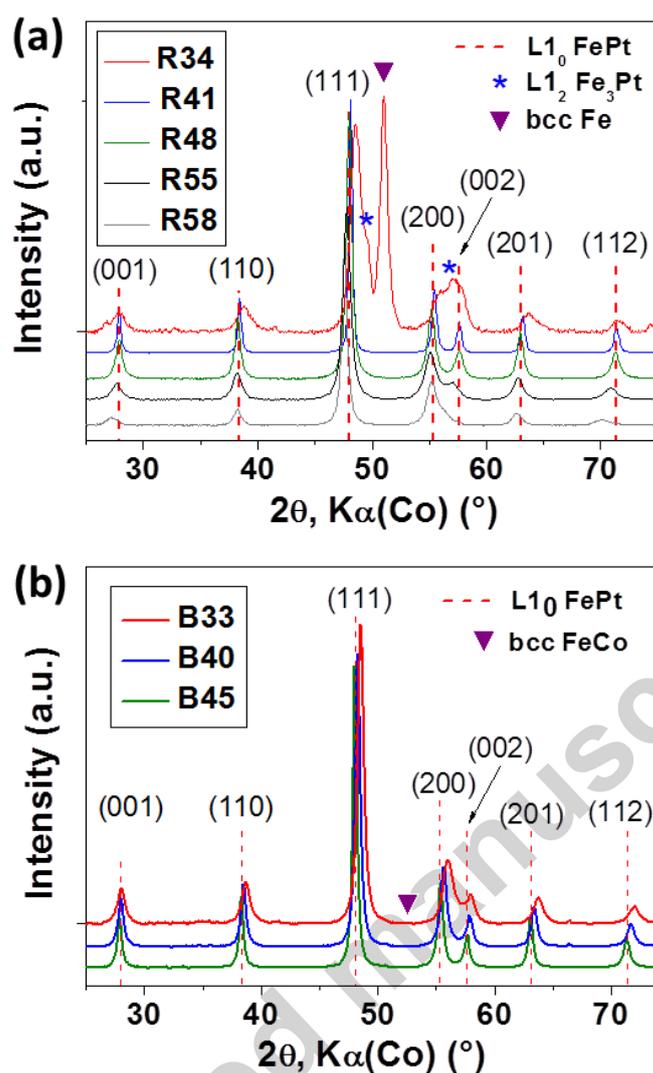
Figure 3. XRD patterns of (a) FePt NPs with various compositions, (b) composites B45 ($Fe_{49}Co_6Pt_{45}$), B40 ($Fe_{48}Co_{12}Pt_{40}$) and B33 ($Fe_{50}Co_{17}Pt_{33}$) after 1h annealing at 650°C under forming gas.

High ordering factors S_1 (eq.(2)) were determined revealing a high degree of conversion (table 2). The S_1 could not be calculated for R34 samples due to the superimposition of the additional phases. The *a* and *c* lattice parameters were determined as they provide information on both the ordering and the incorporation of Fe or Co elements as previously shown theoretically [34,35] and experimentally [36,37]. When the proportion of FeCo introduced in the composites increases, both *a* and *c* parameters deduced from the XRD diminish (table 2), indicating a gradual incorporation of light atoms in the *L1₀* phase [36].

11

Samples	R48	B45	R41	B40	R34	B33
Composition (%at.)	$Fe_{52}Pt_{48}$	$Fe_{49}Co_6Pt_{45}$	$Fe_{59}Pt_{41}$	$Fe_{48}Co_{12}Pt_{40}$	$Fe_{66}Pt_{34}$	$Fe_{50}Co_{17}Pt_{33}$
$a_{(200)}$ (Å)	3.866	3.857	3.852	3.839	3.815	3.816
$c_{(001)}$ (Å)	3.716	3.718	3.715	3.704	3.710	3.699
S_1	0.96	0.91	0.94	0.92	-	0.88

Table 2. Parameters a and c calculated from (200) and (001) peak positions respectively and ordering factor S_1 of the tetragonal $L1_0$ phase calculated from equation (2). Bx and Rx referred to samples prepared from binary assemblies of FeCo-FePt NPs and the corresponding FePt NPs reference, respectively.

Local chemical mappings were performed using STEM-EDX analyses on annealed FePt-FeCo composites. As expected, strong sintering occurred during annealing, yielding sub-micrometric grains (figure 4a). Homogeneous distribution at the nanometric scale of Fe, Co and Pt elements was evidenced (figure 4b-d).
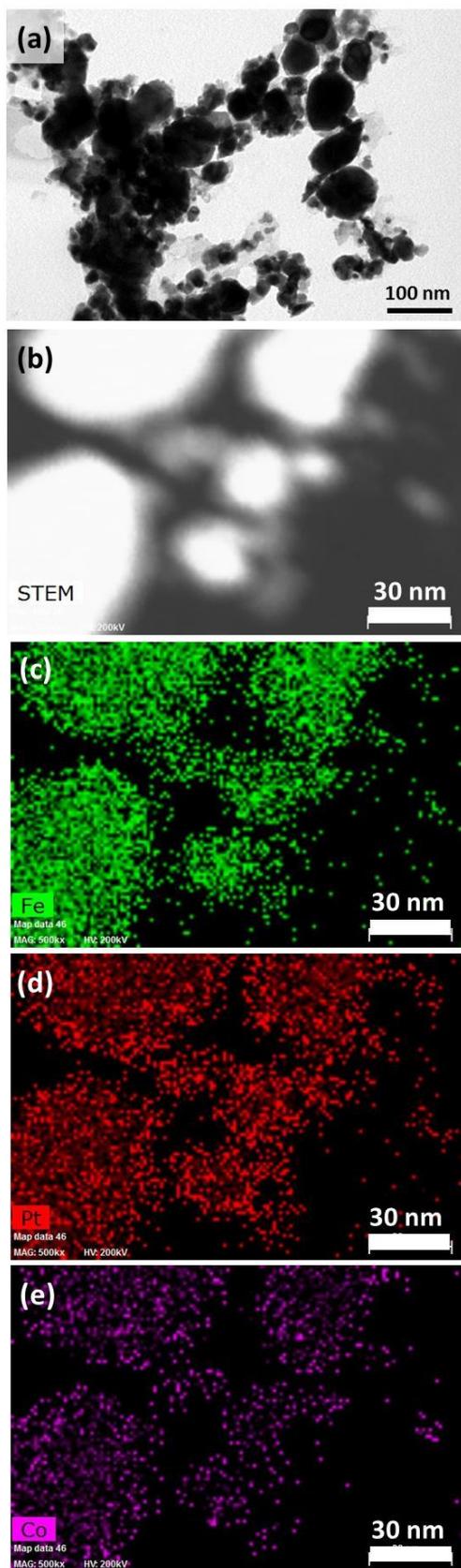
Figure 4. (a) TEM image of annealed B33. (b) STEM-HAADF and the corresponding (c) STEM-EDX chemical mapping of (b) Fe, (c) Pt and (d) Co elements on adjacent grains.

3.2.2. Magnetic characterization

3.2.2.1. Hysteresis curves. Figure 5a shows the hysteresis curves recorded at room temperature of the three binary assemblies (B45, B40 and B33) and the corresponding references (R48, R41 and R34), with fairly similar atomic Pt contents. All samples exhibit a very open single-step hysteresis loops, as a result of the $L1_0$ FePt ordering, with the exception of R34. The presence of additional soft phases $L1_2$ Fe_3Pt and *bcc* FePt indeed induced a drastic reduction of the coercivity ($\mu_0Hc = 0.3$ T).
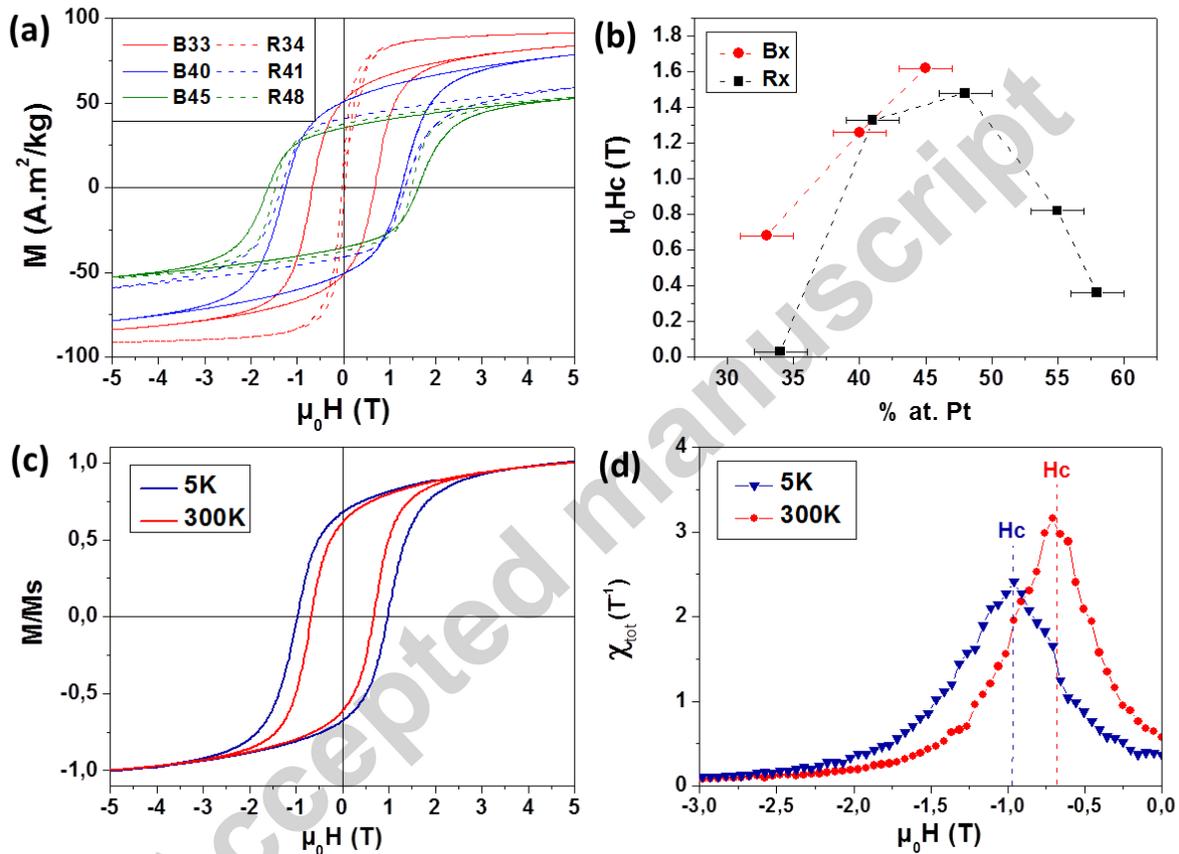

Figure 5. (a) Hysteresis cycle measured at 300K for annealed B45, B40, B33 composites and the corresponding R48, R41 and R34 references. (b) Evolution of the coercivity H_c. (c) Hysteresis cycles and (d) total susceptibility measured at 300K and 5K on annealed B33. Dashed lines : coercive field.

As expected, the magnetization measured at 5T, referred to from now as *M-5T*, kept on increasing when the Pt content decreased in the assemblies and the corresponding references (figure S4 in SI). The evolution of the coercivity as a function of the Pt content observed in pure FePt NPs (figure 5b) was however non monotonic and could be explained by the modification of the magnetocrystalline

anisotropy of the $L1_0$-phase with the composition, the maximum being expected for $Fe_{55}Pt_{45}$ [36,38]. Even if a similar trend was observed for the binary assemblies, due to interdiffusion process, the B33 sample was outstanding (table 3). Indeed, coercivities of $\mu_0H_C = 0.7$ T and 0.97T were measured at 300K and 5K, respectively, far above the values of the R34 reference (figure 5c). The total susceptibility curves, which correspond to the slope of the demagnetization curve in the second and third quadrants, were determined (figure 5d). For comparison purpose, we normalized this susceptibility by the remanent magnetization (*Mr*) as follows :

$$\chi_{\text{tot}}(-\text{Hi}) = \frac{1}{M_r} \left.\frac{d\text{M(H)}}{d\text{H}}\right|_{\text{H}=-\text{Hi}} \qquad (9)$$

The normalized susceptibility exhibits a single maximum at the coercive field, evidencing a single-step reversal of magnetization in the B33 composite at 5 and 300 K.

3.2.2.2. DC demagnetization, Recoil curves. Though less studied than Henkel plots and δM plots, recoil curves, recorded during DC demagnetization (DCD) process, give information on the reversibility of the magnetization reversal of a material and thus on the presence of interphase exchange coupling in multiphasic materials [4,7,39,40].

Recoil curves were fairly flat for B45 and B40 samples. B33 exhibit a slightly steeper shape, expected in spring magnets [15]. The recoil loops are rather closed as in monophasic magnets, except for B33 sample, which contains the highest FeCo content (figure 6b and S5 in SI).
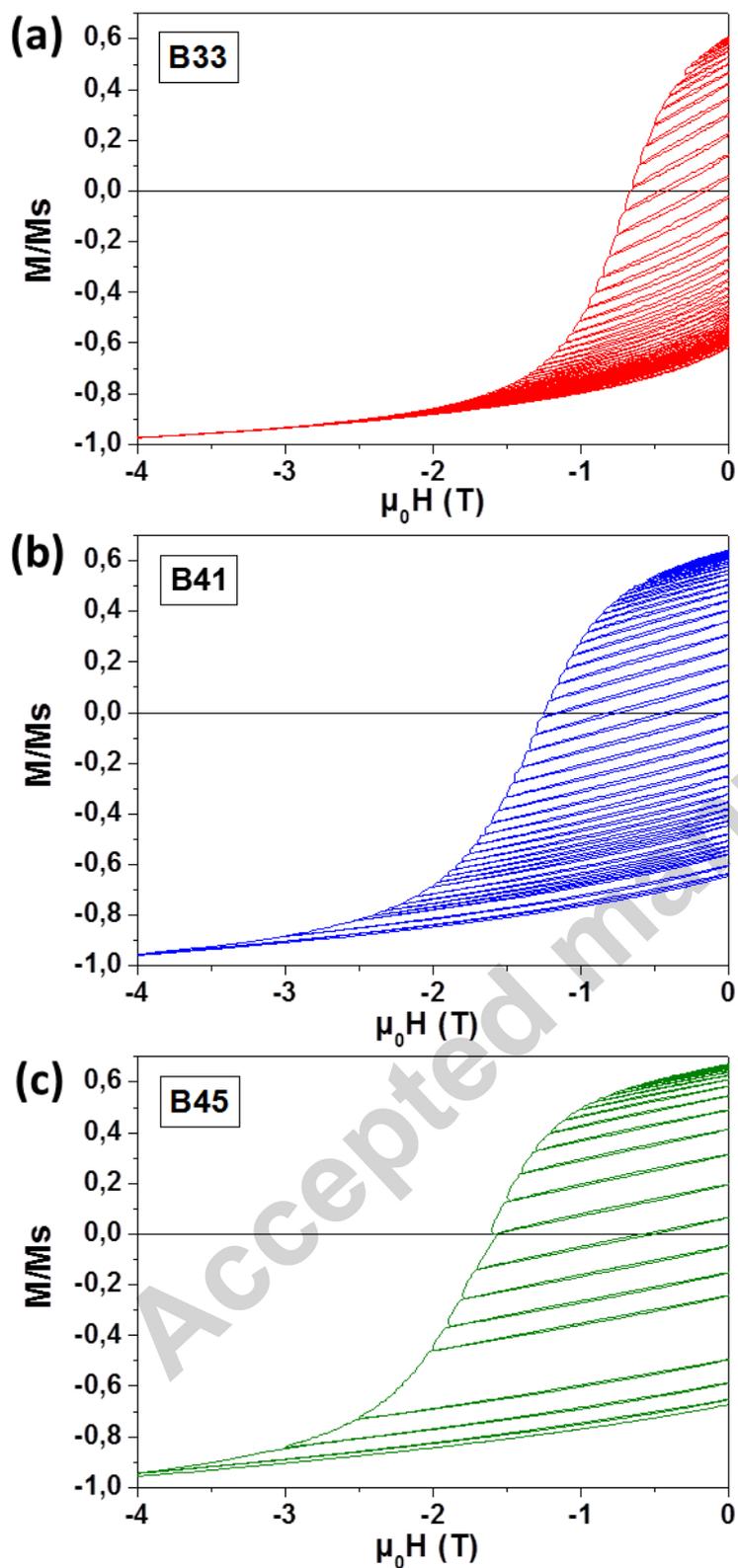
Figure 6. DCD measurements at 300K of (a) B33, (b) B40 and (c) B45 samples. The measurements have been performed at a constant magnetic field sweep rate of 10 mT/s.

The evolution of the normalized recoverable magnetizations m_{rec} as a function of the reduced applied field H/H_c is plotted in figure 7a. The presence of exchange coupling between hard and soft grains should induce a clear maximum in the m_{rec}=f(H/Hc) curve, close to the coercivity. Indeed, the so-called spring effect consists in the reversible reversal of the soft moments under the applied field ($-H_i$). When the field returns to zero, the soft moments will flip back to their initial position, due to the coupling with the hard phase moments, leading to an important recoverable magnetization M_{rec}. This effect reaches its maximum just before the irreversible rotation of the hard phase moments starts, i.e. slightly below the coercive field [4,15]. However, none of our composites exhibit clearly such feature. Instead, a fairly constant increase, close to the expected behavior of single-phase magnets, was evidenced. A slope change is however observed around the coercivity, the amplitude of which increases with the proportion of FeCo introduced. This effect is highlighted by the recoverable susceptibility χ_{rec} which presents a clear maximum around the coercivity (figure 7b).
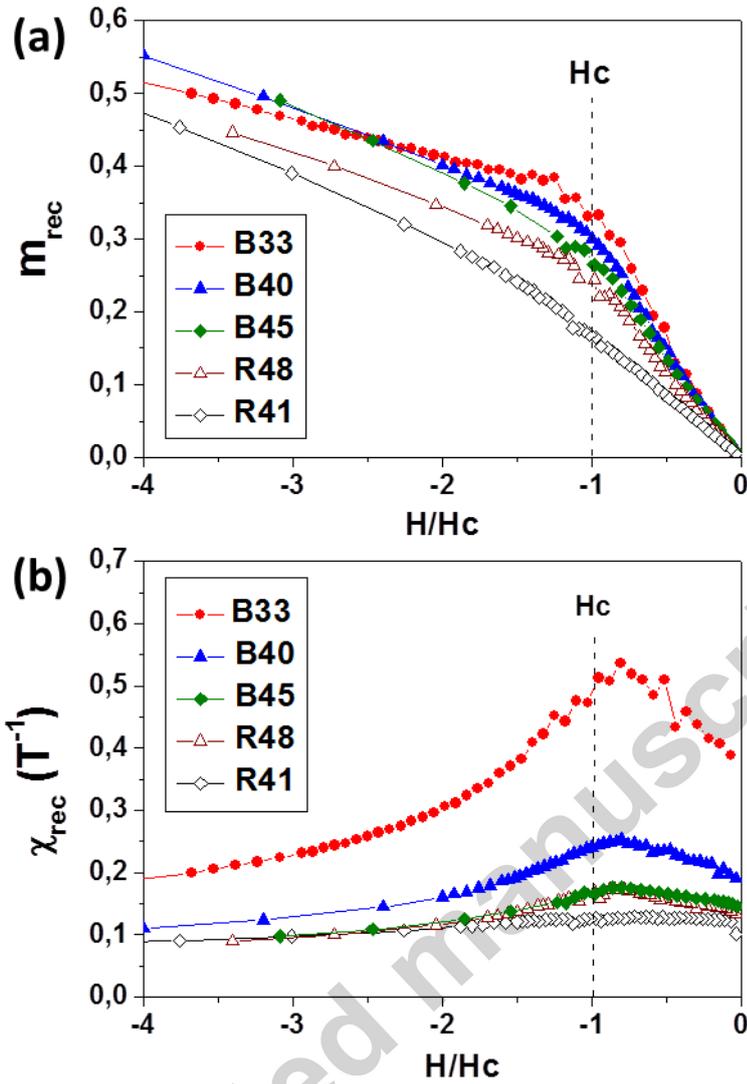
Figure 7. (a) m_{rec} and (b) χ_{rec} as a function of *H/Hc* for B45, B40, B33 assemblies and R48 and R41 references after a 1 h annealing at 650°C under *forming gas*. Dashed lines : coercive field.

3.2.2.3. Contribution of the reversible susceptibility to the total susceptibility. Another way of characterizing the presence of exchange coupling between hard and soft grains consists in evaluating the reversibility of the magnetization reversal process. To do so, the reversible susceptibility χ_{rev}, measured as the initial slope of the recoil curves, is compared to the total susceptibility χ_{tot}, calculated as the derivative of the demagnetization curve (figure 8). χ_{rev}/χ_{tot} ratio were determined for the different samples, except for R34 due to its soft magnetic character. For pure FePt references, the χ_{rev}/χ_{tot} ratio falls in the range 4-5%, in agreement with previous reports on single phase magnets

18

[15,41]. This ratio increases with the FeCo content of the composites, reaching a maximum of 17% for B33 (table 3). Such ratio is an intermediate between the single phase behavior and the typical spring magnets, for which ratios varying from 30 to 40% have been previously measured [15,41].
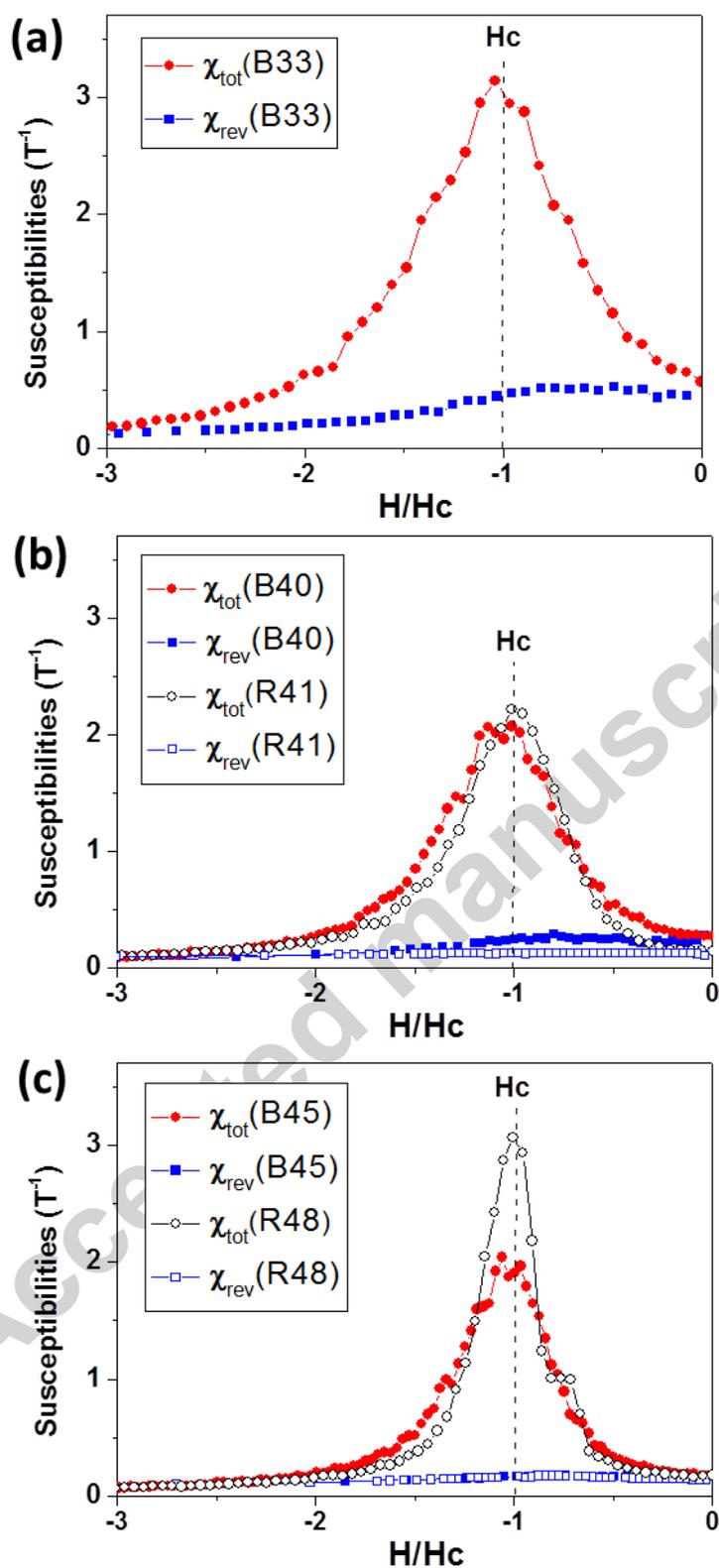
Figure 8. χ_{tot} (red dots) and χ_{rev} (blue squares) susceptibilities as a function of the applied field for (a) B33, (b) B40 and (c) B45 samples. The reference R41 and R48 were inserted in b and c for direct comparison (empty symbols). Dashed line : coercive field.

Samples	R48	B45	R41	B40	R34	B33
Composition (%at.)	$Fe_{52}Pt_{48}$	$Fe_{49}Co_6Pt_{45}$	$Fe_{59}Pt_{41}$	$Fe_{48}Co_{12}Pt_{40}$	$Fe_{66}Pt_{34}$	$Fe_{50}Co_{17}Pt_{33}$
$\mu_0 H_C$ (T)	1.5	1.6	1.2	1.2	0.3	0.7
M-5T (A.m^2/kg)	53	53	59	79	91	84
χ_{rev}/χ_{tot} (%)	6	9	6	14	-	17
$(BH)_{max}$ (kJ/m^3)	100	70	90	132	~ 0	95

Table 3. Coercive field ($\mu_0 H_C$), magnetic moment measured for an applied field $\mu_0 H = 5T$ (M_s), reversible contribution of the susceptibility (χ_{rev}/χ_{tot}) and energy product $(BH)_{max}$ of annealed samples prepared from binary assemblies of FeCo-FePt NPs and the corresponding FePt NPs references (300K).

3.2.3. Performance assessment. The maximum energy product, known as $(BH)_{max}$, is the figure of merit of permanent magnets. $(BH)_{max}$ can be deduced from the measured hysteresis loops providing some assumptions on the material studied. If one considers that the material is dense, which is not strictly relevant in our case since measurements were performed on manually compacted powders, induction loops $B(H)=\mu_0(H+M)$ can be derived from the magnetization loops M=f(H) taking into account a mean volume fraction of the composite (see Experimental section). The evolution of the energy product (BH) can then be calculated, the maximum of which corresponds to the $(BH)_{max}$, indicating the optimal working point of the magnet (figure 9a).

The $(BH)_{max}$ values are reported as a function of the Pt content in the assemblies (red dots) and in the starting FePt NPs treated under the same conditions (black squares) in figure 9b.
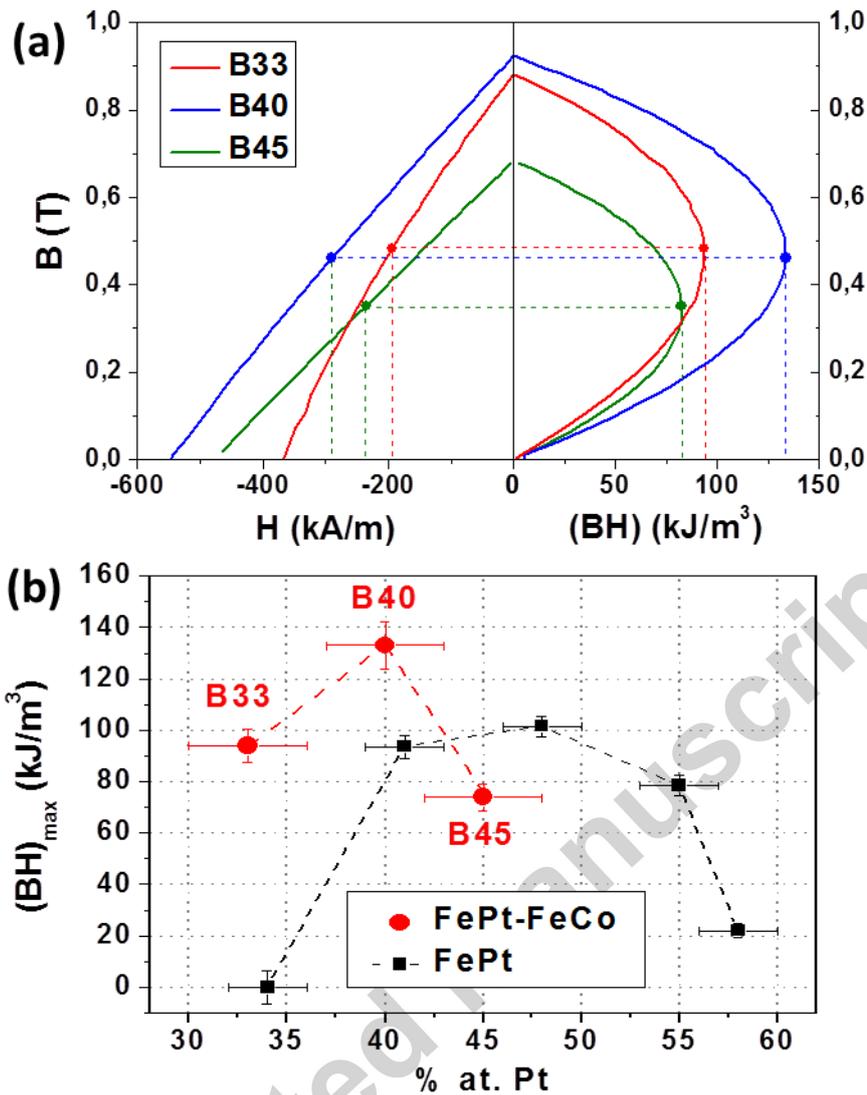
Figure 9. (a) 2nd quadrant of the induction loops and corresponding (BH) curves for the FePt-FeCo assemblies. The dots correspond to the (BH)$_{max}$ position and the optimum working point. (b) Evolution of (BH)$_{max}$ as a function of the Pt content in the FeCo/FePt composites (red dots) and the FePt references (black squares).

Binary assemblies of FeCo/FePt NPs, after thermal annealing, reached higher (BH)$_{max}$ values than pure FePt NPs. Remarkably, (BH)$_{max}$ values close to 100 kJ/m^3 could be estimated for B33 which only contains 33% of platinum. Moreover, an optimum (BH)$_{max}$ value of 133 kJ/m^3 could be estimated for sample B40. Such value is similar to the one reported by Chaubey *et al.* on a *L1$_0$* FePt/*bcc* FeCo composite (123 kJ/m^3) obtained from *fcc* FePt/CoFe$_2$O$_4$ heterodimers annealed at 700°C [33].

22

4. Discussion

The preparation of exchange-coupled magnets based on a bottom-up approach was not as widely studied as one could expect based on the promising results obtained in 2002 by Zeng *et al*.[21]. Several challenges should indeed be overcome to obtain an efficient exchange coupling between chemically grown nanoparticles. Among them, the presence of large soft grain domains in the final material being detrimental to an effective exchange-coupling [8], the optimization of the self-assembly of binary mixtures is a key parameter. Intensive works have been dedicated to the controlled self-assembly of binary nanospheres to design new multifunctional materials [42,43]. In our case, a simple ligand-exchange process using 4-mercapto benzoic acid could induce a fairly homogeneous distribution of FeCo and FePt nanoparticles within assemblies. Colloidal solutions could easily promote binary assemblies while decreasing the amount of organic matter, without facing any phase separation issues even for the highest FeCo content introduced (34% at.).

Another challenge consists in preserving the homogeneous size distribution during thermal annealing. Indeed, the high temperature required to convert *fcc* FePt NPs into hard $L1_0$ phase may promote sintering and interdiffusion between adjacent nanoparticles. This interdiffusion is a major drawback since the proportion of the soft phase in the final material may dramatically shrink and could not be precisely controlled (figure 9). In our case, the treatment at 650°C under forming gas induced the total dissolution of the FeCo nanoparticles into a $L1_0$-$Fe_{49}Co_6Pt_{45}$ phase for sample B45, which exhibits the same magnetic and structural properties than pure $Fe_{52}Pt_{48}$ NPs (R48).

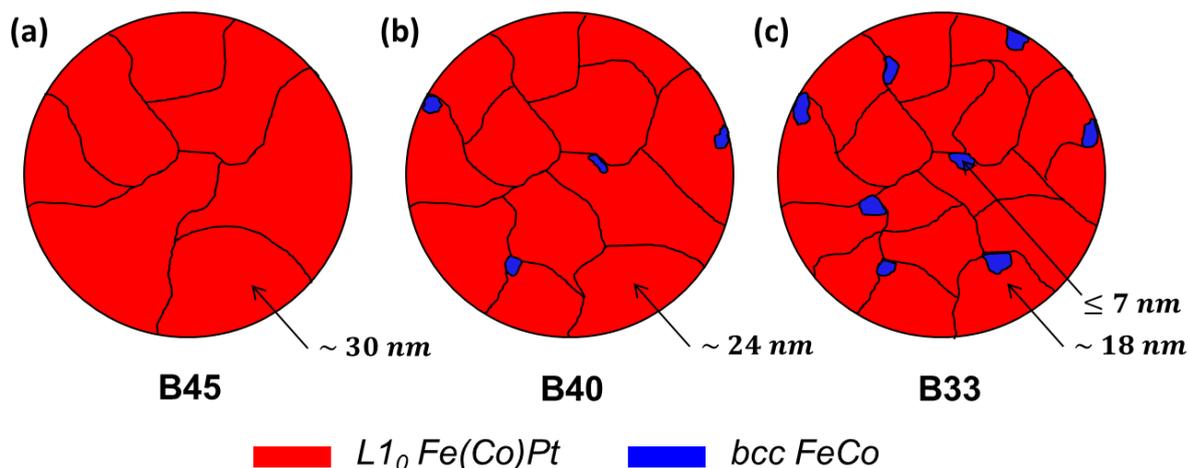**Figure 10.** Schematic view of the polycrystalline particles for the assemblies (a) B45 ($Fe_{49}Co_6Pt_{45}$), (b) B40 ($Fe_{48}Co_{12}Pt_{40}$) and (c) B33 ($Fe_{50}Co_{17}Pt_{33}$) made from *fcc* FePt and *bcc* NPs FeCo after a 1h annealing at 650°C under *forming gas*. (Red : $L1_0$ Fe(Co)Pt, blue : *bcc* FeCo). The sizes indicate the crystallite mean size deduced from XRD.

When the proportion of FeCo introduced increases, the changes of the magnetic properties compared to pure FePt materials become significant. Magnetic analyses suggest that samples B40 and B33 may be composed in majority of an hard $L1_0$ (FeCo)Pt phase coupled by an interphase exchange coupling to a soft FeCo phase. The recoverable magnetization and reversible susceptibility evidence an intermediate state between a pure single phase, as B45, and a spring-magnet. Though the reversibility is still far from the optimized values for spring-magnets ($\chi_{rev}/\chi_{tot} \approx 40\%$), the presence of a small fraction of soft phase is sufficient to enhance the saturation magnetization of the materials and thus increase the $(BH)_{max}$ compared to pure FePt materials.

To further improve the nanocomposites obtained, interdiffusion of the different phases should be prevented, in order to maintain a high fraction of soft phase and a high magnetocrystalline anisotropy of the hard phase. To do so, the annealing temperature should be drastically lowered while the conversion of the FePt towards the $L1_0$ hard phase is maintained. Studies on thin films have shown that addition of a third chemical element such as Sb, Sn, Cu, Ag, Au, etc. in the 3d-5d alloys can significantly reduce the ordering temperature [44]. Though well studied in thin films, only few reports can be found on ternary FePtX NPs prepared by wet chemistry. FePtSb [45] and FePtAu NPs [46] could be converted into a hard magnetic phase exhibiting a coercive field close to 1T after an annealing at

only 400°C. Thus, one strategy to avoid strong diffusion would consist in mixing FeCo NPs with FePtX NPs and perform a thermal annealing at temperatures as low as 400°C. Optimization of the FePtX NPs synthesis is however mandatory to ensure a better stabilization and size homogeneity.

An alternative approach consists in separating the conversion of the *fcc* FePt phase from the formation of a metallic interface between adjacent grains. Indeed, well stabilized $L1_0$-FePt nanoparticles could be prepared through a multi-step process involving soluble NaCl [47], SiO$_2$ [48] or MgO matrix [49]. This matrix acts as a barrier to prevent the coalescence of NPs during thermal annealing while the $L1_0$-FePt NPs can be then stabilized in organic solvents by addition of long chain surfactants during the matrix removal [24]. Composites prepared from *bcc* FeCo and $L1_0$-FePt could thus be prepared. Annealing at low temperatures would ensure intermetallic interfaces between adjacent hard and soft grains.

5. Conclusion

We reported here a systematic study on the structural and magnetic properties of nanostructured materials prepared from binary assemblies of FeCo and FePt nanoparticles and the comparison with pure FePt materials. The use of a bifunctional mercapto benzoic acid enabled us to obtain homogeneous assemblies of the two types of particles in a fairly easy way. Thermal annealing performed at 650°C led to the important interdiffusion of FeCo into FePt phases, decreasing drastically the amount of soft phase present in the final composites. Despite this interdiffusion, the analysis of recoil curves evidenced the presence of an efficient interphase exchange coupling which enhanced the magnetic performances (BH)$_{max}$.

To further control the structural and magnetic properties of the composite material, the use of FePtX or $L1_0$-FePt NPs is now required to decrease the annealing temperature and thus prevent the interdiffusion. Though only few reports have been mentioned the interest in bottom-up approach for spring-magnets, we believe that chemically grown nanoparticles offer a very promising way to yield subcentimetric magnets with optimized properties.

Acknowledgments :

Supplementary Informations :

Supplementary material, structural and magnetic characterization of the starting NPs and the obtained assemblies, is available in the online version of this article at http:

/**********************

References :

(1) Chen, P.; Huang, Y.-Y.; Hoshino, K.; Zhang, J. X. J. *Sci. Rep.* **2015**, *5*, 8745.

(2) Arnold, D. P. *IEEE Trans. Magn.* **2007**, *43* (11), 3940.

(3) Gutfleisch, O.; Willard, M. A.; Brück, E.; Chen, C. H.; Sankar, S. G.; Liu, J. P. *Adv. Mater.* **2011**, *23* (7), 821.

(4) Kneller, E. F.; Hawig, R. *Magn. IEEE Trans. On* **1991**, *27* (4), 3588.

(5) Coey, J. M. D. *Magnetism and magnetic materials*; Cambridge University Press: Cambridge, 2010.

(6) Skomski, R. *J. Phys. Condens. Matter* **2003**, *15* (20), R841.

(7) Hadjipanayis, G. C. *J. Magn. Magn. Mater.* **1999**, *200*, 373.

(8) Skomski, R.; Coey, J. M. D. *Phys. Rev. B* **1993**, *48* (21), 15812.

(9) Schrefl, T.; Fidler, J.; Kronmüller, H. *Phys. Rev. B* **1994**, *49* (9), 6100.

(10) Shan, Z. S.; Liu, J. P.; Chakka, V. M.; Zeng, H.; Jiang, J. S. *IEEE Trans. Magn.* **2002**, *38* (5), 2907.

(11) Guo, Z. J.; Jiang, J. S.; Pearson, J. E.; Bader, S. D.; Liu, J. P. *Appl. Phys. Lett.* **2002**, *81* (11), 2029.

(12) Asti, G.; Solzi, M.; Ghidini, M.; Neri, F. M. *Phys. Rev. B* **2004**, *69* (17), 174401.

(13) Bader, S. D. *Rev. Mod. Phys.* **2006**, *78* (1), 1.

(14) Coehoorn, R.; De Mooij, D. B.; de Waard, C. de. *J. Magn. Magn. Mater.* **1989**, *80* (1), 101.

(15) Feutrill, E. H.; McCormick, P. G.; Street, R. *J. Phys. Appl. Phys.* **1996**, *29* (9), 2320.

(16) Liu, F.; Hou, Y.; Gao, S. *Chem. Soc. Rev.* **2014**.
(17) Poudyal, N.; Ping Liu, J. *J. Phys. Appl. Phys.* **2013**, *46* (4), 43001.
(18) Saravanan, P.; Hsu, J.-H.; Reddy, G. L. N.; Kumar, S.; Kamat, S. V. *J. Alloys Compd.* **2013**, *574*, 191.
(19) Choi, Y.; Jiang, J. S.; Ding, Y.; Rosenberg, R. A.; Pearson, J. E.; Bader, S. D.; Zambano, A.; Murakami, M.; Takeuchi, I.; Wang, Z. L.; Liu, J. P. *Phys. Rev. B* **2007**, *75* (10).
(20) Liu, Y.; George, T. A.; Skomski, R.; Sellmyer, D. J. *Appl. Phys. Lett.* **2011**, *99* (17), 172504.
(21) Zeng, H.; Li, J.; Liu, J. P.; Zhong, L. W.; Sun, S. *Nature* **2002**, *420* (6914), 395.
(22) López-Ortega, A.; Estrader, M.; Salazar-Alvarez, G.; Roca, A. G.; Nogués, J. *Phys. Rep.* **2015**, *553*, 1.
(23) Zeng, H.; Li, J.; Wang, Z. L.; Liu, J. P.; Sun, S. *Nano Lett.* **2004**, *4* (1), 187.
(24) Liu, F.; Zhu, J.; Yang, W.; Dong, Y.; Hou, Y.; Zhang, C.; Yin, H.; Sun, S. *Angew. Chem. Int. Ed.* **2014**, *53* (8), 2176.
(25) Zeng, H.; Sun, S.; Li, J.; Wang, Z. L.; Liu, J. P. *Appl. Phys. Lett.* **2004**, *85* (5), 792.
(26) Rong, C.-B.; Nandwana, V.; Poudyal, N.; Liu, J. P.; Saito, T.; Wu, Y.; Kramer, M. J. *J. Appl. Phys.* **2007**, *101* (9), 09K515.
(27) Lacroix, L.-M.; Lachaize, S.; Falqui, A.; Respaud, M.; Chaudret, B. *J. Am. Chem. Soc.* **2009**, *131* (2), 549.
(28) Christodoulides, J. A.; Farber, P.; Dannl, M.; Okumura, H.; Hadjipanaysi, G. C.; Skumryev, V.; Simopoulos, A.; Weller, D. *Magn. IEEE Trans. On* **2001**, *37* (4), 1292.
(29) Soulantica, K.; Wetz, F.; Maynadié, J.; Falqui, A.; Tan, R. P.; Blon, T.; Chaudret, B.; Respaud, M. *Appl. Phys. Lett.* **2009**, *95* (15), 152504.
(30) Li, Z. B.; Shen, B. G.; Sun, J. R. *J. Appl. Phys.* **2013**, *113* (1), 13902.
(31) Zheng, B.; Zhang, H.-W.; Zhao, S.; Chen, J.; Wu, G. *Appl. Phys. Lett.* **2008**, *93* (18), 182503.
(32) Bagaria, H. G.; Ada, E. T.; Shamsuzzoha, M.; Nikles, D. E.; Johnson, D. T. *Langmuir* **2006**, *22*, 7732.
(33) Chaubey, G. S.; Nandwana, V.; Poudyal, N.; Rong, C.; Liu, J. P. *Chem. Mater.* **2008**, *20* (2), 475.
(34) Berry, D. C.; Barmak, K. *J. Appl. Phys.* **2007**, *101* (1), 14905.
(35) Ho, H.; Laughlin, D. E.; Zhu, J.-G. *IEEE Trans. Magn.* **2012**, *48* (11), 2749.
(36) Barmak, K.; Kim, J.; Lewis, L. H.; Coffey, K. R.; Toney, M. F.; Kellock, A. J.; Thiele, J.-U. *J. Appl. Phys.* **2005**, *98* (3), 33904.
(37) Klemmer, T. J.; Shukla, N.; Liu, C.; Wu, X. W.; Svedberg, E. B.; Mryasov, O.; Chantrell, R. W.; Weller, D.; Tanase, M.; Laughlin, D. E. *Appl. Phys. Lett.* **2002**, *81* (12), 2220.
(38) Sun, S.; Fullerton, E. E.; Weller, D.; Murray, C. B. *Magn. IEEE Trans. On* **2001**, *37* (4), 1239.
(39) Lyubina, J.; Opahle, I.; Müller, K.-H.; Gutfleisch, O.; Richter, M.; Wolf, M.; Schultz, L. *J. Phys. Condens. Matter* **2005**, *17* (26), 4157.
(40) Emura, M.; Cornejo, D. R.; Missell, F. P. *J. Appl. Phys.* **2000**, *87* (3), 1387.
(41) Cornejo, D. R.; Villas-Boas, V.; Missell, F. P. *J. Appl. Phys.* **1998**, *83* (11), 6637.
(42) Redl, F. X.; Cho, K.-S.; Murray, C. B.; O'Brien, S. *Nature* **2003**, *423*, 968.
(43) Shevchenko, E. V.; Talapin, D. V.; Kotov, N. A.; O'Brien, S.; Murray, C. B. *Nature* **2006**, *439* (7072), 55.
(44) Maeda, T.; Kai, T.; Kikitsu, A.; Nagase, T.; Akiyama, J. *Appl. Phys. Lett.* **2002**, *80* (12), 2147.
(45) Yan, Q.; Kim, T.; Purkayastha, A.; Ganesan, P. G.; Shima, M.; Ramanath, G. *Adv. Mater.* **2005**, *17* (18), 2233.
(46) Nandwana, V.; Chaubey, G. S.; Zhang, Y.; Liu, J. P. *J. Nanosci. Nanotechnol.* **2010**, *10* (5), 2979.
(47) Delattre, A.; Pouget, S.; Jacquot, J.-F.; Samson, Y.; Reiss, P. *Small* **2010**, *6* (8), 932.
(48) Tamada, Y.; Yamamoto, S.; Takano, M.; Nasu, S.; Ono, T. *Appl. Phys. Lett.* **2007**, *90* (16), 162509.
(49) Kim, J.; Rong, C.; Liu, J. P.; Sun, S. *Adv. Mater.* **2009**, *21* (8), 906.

Graphical abstract